

Use of an elasto-plastic model and strain measurements of embedded fibre Bragg grating sensors to detect Mode I delamination crack propagation in woven cloth (0/90) composite materials

Ayad Arab Kakei^{1,2}, Mainul Islam¹,
Jinsong Leng^{3,4} and Jayantha A Epaarachchi¹

Abstract

Mode I fracture analysis being employed to study delamination damage in fibre-reinforced composite structures under in-plane and out-of-plane load applications. However, due to the significantly low yield strength of the matrix material and the infinitesimal thickness of the interface matrix layer, the actual delamination process can be assumed as a partially plastic process (elasto-plastic). A simple elasto-plastic model based on the strain field in the vicinity of the crack front was developed for Mode I crack propagation. In this study, a double cantilever beam experiment has been performed to study the proposed process using a 0/90-glass woven cloth sample. A fibre Bragg grating sensor has embedded closer to the delamination to measure the strain at the vicinity of the crack front. Strain energy release rate was calculated according to ASTM D5528. The model predictions were comparable with the calculated values according to ASTM D5528. Subsequently, a finite element analysis on Abaqus was performed using 'Cohesive Elements' to study the proposed elasto-plastic behaviour. The finite element analysis results have shown a very good correlation with double cantilever beam experimental results, and therefore, it can be concluded that Mode I delamination process of an fibre-reinforced polymer composite can be monitored successfully using an integral approach of fibre Bragg grating sensors measurements and the prediction of a newly proposed elasto-plastic model for Mode I delamination process.

Keywords

Mode I fracture, elasto-plastic model, composite, delamination, fibre Bragg grating sensors

Introduction

Laminated glass fibre-reinforced polymer (GFRP) composites have been widely used as structural components in different fields of engineering applications due to their mechanical properties such as excellent strength/weight ratio, easy formability, geometrical stability and corrosion resistance. Composite reinforcements offer many other advantages, when made as textile glass fibre mats such as woven fabrics. Some of these advantages include ease of handling for mechanisation, ability to conform complex shapes and improved fracture toughness.

Although composite materials present great advantages, laminated composite structures are damage

susceptible and involve distinct damage modes, such as transverse cracks, interfacial debonding, matrix crack,

¹Centre for Future Materials, University of Southern Queensland, Toowoomba, QLD, Australia

²College of Engineering, University of Kirkuk, Kirkuk, Iraq

³School of Mechanical and Electrical Engineering and Centre of Excellence in Engineered Fibre Composites, University of Southern Queensland, Toowoomba, QLD, Australia

⁴Centre for Smart Materials and Structures, School of Astronautics, Harbin Institute of Technology, Harbin, China

Corresponding author:

Jayantha A Epaarachchi, Centre for Future Materials, University of Southern Queensland, West Street, Toowoomba, QLD 4350, Australia.
Email: eparracj@usq.edu.au

delamination and fibre breakage. Delamination is the most common failure in composite structures and has harmful effects on structural integrity.¹ For example, Pawar and Ganguli² have observed the loss of bending and torsion stiffness due to extent of delamination to be 40%–45% in a thin-walled composite beam of helicopter rotor blade. As such, comprehensive understanding and characterising of delamination crack initiation and the propagation are the essential fundamental knowledge of structural durability and damage tolerance evaluation for composites.

Both experimental characterisation and prediction of delamination damage response are prohibitively complicated due to non-homogeneous properties of composite structures. Due to this reason, many theoretical, numerical and experimental efforts have been devoted over the past years to the characterisation and prediction of delamination in composites. Suppakul and Bandyopadhyay³ have investigated the influence of the weave pattern on Mode I interlaminar fracture energy of glass/vinyl ester laminates. They have found that the weave pattern has a significant influence on the initial fracture energy (G_{IC}). In a study by Pereira et al.,⁴ it has shown experimentally and numerically the effect of inter-ply damage and delamination crack branching to a neighbouring interface crack on initial fracture energy (G_{IC}). They have used the data from a double cantilever beam (DCB) test of woven fabric glass/epoxy multi directional (MD) specimen. The results show that inter-ply and delamination crack branched to another interface because of non-midplane of delamination crack propagation. Although the crack propagation phenomena do not prevent the measurement of initial G_{IC} , it has a significant influence on R -curve value. This finding has warranted additional care about material dependent effects on the determination of fracture toughness of composites.

Recent advances in fibre optic sensor technologies have provided great opportunities to develop techniques for characterising and detecting delamination initiation and propagation in composite materials.^{5,6} There have been many types of research works on detecting internal damage in composite structures using fibre Bragg grating (FBG) sensors. Yashiro et al.⁷ have investigated the relationship between the multiple damage states of the laminate and the complicated reflection spectrum of the FBG sensor using a numerical model which maps strain field around the damaged region. They have concluded that the FBG sensor spectra have significantly changed relative to the crack size. Sans et al.⁸ have used 8-mm-long FBG sensors to locate the crack tip in a carbon/epoxy unidirectional sample which was subjected to mixed-mode fracture situation. It was found that an axial strain field measured within the grating can be used to determine the location

of the crack tip precisely with the FBG sensors. Okabe and Yashiro⁹ have analysed the reflected spectrum of embedded FBG sensors using a strain field simulated by layer-wise finite element analysis (FEA) using cohesive elements for damage extension in single-holed carbon fibre-reinforced polymer (CFRP)-laminated plate under static and fatigue loading. Takeda et al.¹⁰ have studied the quantitative detection of delamination in CFRP cross-ply laminates under 4-point bending test using the small-diameter FBG sensor. Then, Takeda et al.¹¹ have applied the small-diameter FBG sensors to monitor delamination size in the CFRP laminates subjected to low-velocity impact. Sorensen et al.¹² have used FBG strain data to characterise fibre bridging tractions during delamination using long FBG sensors which were embedded parallel to the delamination plane in DCB specimens. Stutz et al.¹³ have used an array of several short FBG sensors to measure the strain fields in the proximity of the delamination crack tip under monotonic and fatigue loadings. Kahandawa et al.^{14,15} have revealed a novel configuration of FBG sensors to acquire strain reading to overcome practical constraints and the engineering challenges associated with FBG-based structural health monitoring (SHM) systems. Kakei et al.¹⁶ have used FBG and thermoelastic stress analysis (TSA) engagement techniques to detect and monitor accumulation damage in glass fibre-reinforced composite under fatigue loading. Yu et al.¹⁷ have used a novel phase-shifted fibre Bragg grating (PS-FBG) system to identify the acoustic emissions (AEs) of damages in a CFRP cross-ply laminate. This research work has shown a great potential for a practical SHM system of CFRP laminates because it takes advantage of the FBG sensor.

Finite element simulation of crack surface

Delamination in composite materials has been widely investigated numerically over many decades. Although there are numerous modelling works available for delamination cracks, the finite element method (FEM) is found to be the most suitable tool for simulation due to the complex nature of delamination problems. The virtual crack closure technique (VCCT) has been utilised in the investigation of delamination in many published studies.^{18,19} The VCCT analysis relies upon two basic hypotheses, namely, the energy released during crack growth is identical to the energy required to close the crack and the stress state at the proximity of the crack does not change significantly when the crack is extended.²⁰ These hypotheses significantly influence the accuracy of the VCCT analysis as it explicitly ignores plasticity in the analysis.¹⁸ In addition, a major drawback of the VCCT method is that it requires a priori knowledge of the initial crack size.²¹ An alternative to

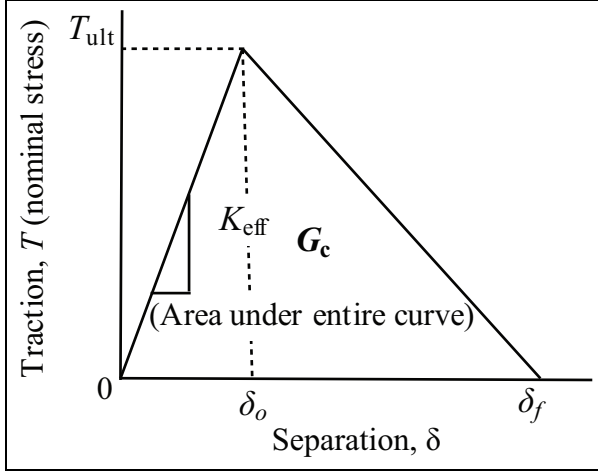


Figure 1. Cohesive parameters of typical bilinear traction-separation model.²⁸

VCCT is the cohesive zone method (CZM), which is becoming more popular in the analysis of delamination in composite materials due to less complex and user-friendly nature.²² The CZM has been used in many studies of delamination crack propagation in composite materials. The cohesive approach is based on the concept of the cohesive crack model. This concept was developed by Barenblatt²³ who introduced cohesive forces in order to solve the equilibrium problem in elastic bodies with cracks. The cohesive damage zone models relate tractions to displacement jumps at an interface when a crack occurs. As shown in Figure 1, the area under the traction–displacement curve is equal to the fracture energy G_c . A probabilistic CZM was developed by Shanmugam et al.²⁴ to capture steady-state energy release rate variations in DCB delamination specimens. Wang and Xu²² have presented an approach using cohesive elements to simulate the propagation of a delamination including both propagation direction and effective propagation length under high-cycle fatigue loading. Saeedifar et al.²⁵ and Haselbach et al.²⁶ have shown that the modified CZM technique has exhibited a good performance in simulating an initiation and propagation of a delamination crack in laminated composite structures. Kakei et al.^{16,27} have used the cohesive element to analyse the delamination damage growth of a $[0/90]_{15}$ woven GFRP composite, and the model provides reasonably accurate results. The aim of this work is to use FBG sensor strain measurements and FEA based on CZM to develop an improved understanding of initiation and propagation of Mode I delamination and establish an elastoplastic mathematical model to evaluate fracture energy (G_I).

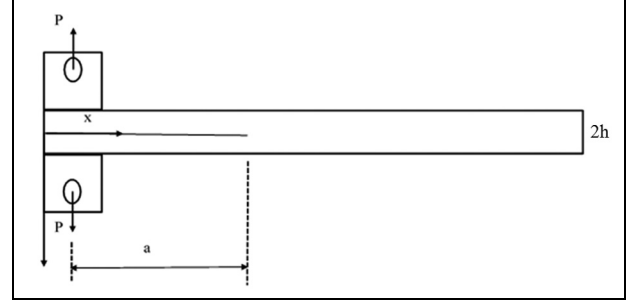


Figure 2. The schematic diagram of a DCB specimen.

Energy release rate in DCB specimens

A schematic of a DCB test is shown in Figure 2, where the specimen thickness is given by $2h$ (mm), the crack length is given by a (mm) and the applied load is given by P (N). The energy release rate in a DCB specimen is defined in a usual way

$$G = \left(\frac{P^2}{2b} \right) \left(\frac{dc}{da} \right) \quad (1)$$

where G is the fracture energy, b (mm) is the width of the specimens, c is the compliance (Δ/P) and a (mm) is length of the delamination crack. Neglecting the bridging effect, the deflection of an ideal cantilever beam,²⁹ which length a (mm), under a load P is given by:

$$v = \frac{P}{I} \left[\frac{(2\bar{S}_{12}\bar{S}_{16} - 3\bar{S}_{12}\bar{S}_{26})b^2}{24\bar{S}_{11}}y - \frac{\bar{S}_{12}}{2}xy^2 + \frac{(-2\bar{S}_{12}\bar{S}_{16} + \bar{S}_{11}\bar{S}_{26})}{6\bar{S}_{11}}y^3 + \frac{\bar{S}_{11}}{6}(x^3 - 3a^2x + 2a^3) \right] \quad (2)$$

where I is the second moment of inertia equals to $4bh^3/3$, and S_{mn} is the compliance coefficient of the beam.³⁰

In order to determine the deflection equation in symmetry, the axis of the beam $y = 0$ is substituted into equation (2) and then simplifying it

$$v = \frac{P\bar{S}_{11}}{I} \frac{1}{6} (x^3 - 3a^2x + 2a^3) \quad (3)$$

or

$$v = \frac{\Delta}{2} \left[\left(\frac{x}{a} \right)^3 - 3 \left(\frac{x}{a} \right) + 2 \right] \quad (4)$$

where $\Delta = Pa^3\bar{S}_{11}/3I$ is the normal displacement of the flexible member from the initial plane, that is, $v(0)$. The full opening (Δ) of the DCB equals the doubled deflection (2Δ), and the popular formula for the DCB is obtained

$$G_I = \frac{3P^2 \bar{S}_{11} a^2}{4b^2 h^3} \quad (5)$$

Elasto-plastic model

After the delamination crack initiation between composite layers, the laminate has divided into two regions. It is reasonable to assume that elastic behaviour in the orthotropic laminate and the plastic behaviour of the epoxy in laminate cause the crack at the tip of delamination as shown in Figure 3.

Due to local bending at the crack front,²⁷ plastic deformation is assumed at the significantly thin interlaminar region (epoxy) near the crack tip at the distance equal to X . The threshold delamination crack length happens in the interlaminar region, for $a = X_Y$ as shown in Figure 4. The beam material has been assumed as perfectly elasto-plastic with yield strength σ_Y as shown in Figure 5. Let y axis be the direction of neutral axis of the beam section, which is measured perpendicularly to the plane of the undeformed beam as shown in Figure 6. The classical Euler–Bernoulli beam relations are assumed, and deformation in the thickness direction is related to the local of curvature by the expression

$$\varepsilon(y) = \frac{y}{R} = y \frac{d^2 y}{dx^2} \quad (6)$$

where $\varepsilon(y)$ is the strain and $1/R$ is the curvature.

The constitutive law for this composite beam (Figure 6) is described by the following equations for stresses:³¹

For orthotropic composite

$$\sigma(y) = E\varepsilon(y) \quad (7)$$

For the matrix-epoxy material, $\varepsilon \geq \varepsilon_{Yepoxy}$

$$\sigma(y) = \sigma_Y \quad (8)$$

The bending moment of upper section is given by

$$M_u = b \int_0^{h/2} \sigma(y) y dy = \frac{bE\varepsilon_{max}^3 R^2}{3} \quad (9)$$

The bending moment of bottom section is given by

$$M_b = b \left[\int_0^{y_Y} \sigma(y) y dy + \int_{y_Y}^{h/2} \sigma_Y y dy \right] \\ = b \left(\frac{E\varepsilon_Y^3 R^2}{3} + \frac{E_{ep}\varepsilon_Y h^2}{4} - \frac{E_{ep}\varepsilon_Y^3 R^2}{2} \right) \quad (10)$$

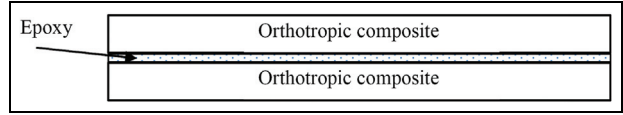


Figure 3. Schematic representation of composite beam as two different materials: one elastic orthotropic composite and the other elastic purely epoxy due to delamination crack.

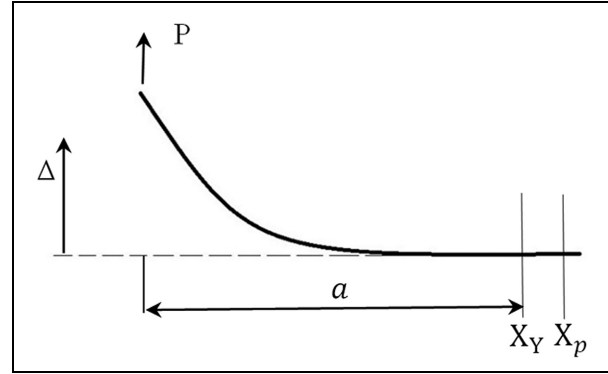


Figure 4. Schematic representation of a part of the beam closer to the crack front which is in the elasto-plastic region.

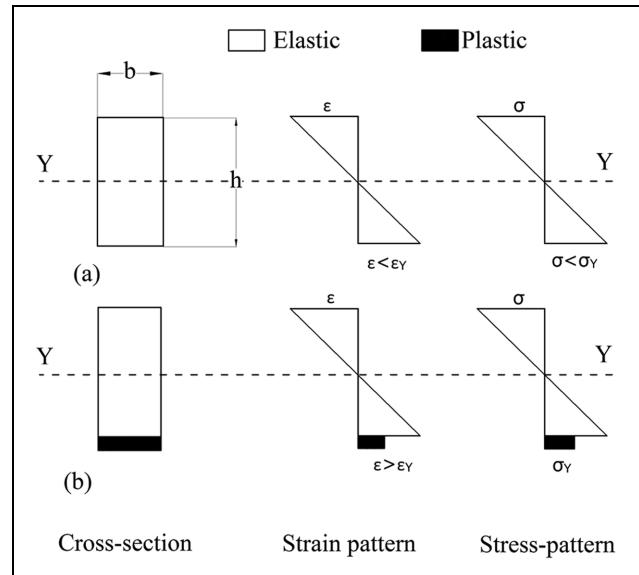


Figure 5. The transition from elastic to plastic state of a cross-section in bending in an interlaminar epoxy layer due to delamination crack (upper-half section): (a) elastic and (b) elasto-plastic.

where E is the Young's modulus of composite specimen, and E_{ep} is Young's modulus of epoxy (matrix). Total moment on the all beam sections is given by

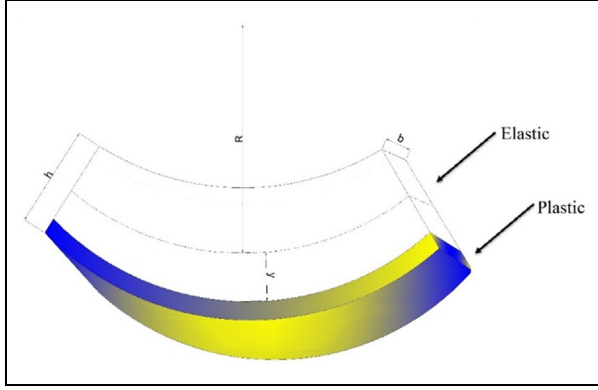


Figure 6. Schematic representation of the composite beam under crack delamination deformation. R corresponds to the radius of curvature (no scale).

$$M = M_u + M_b \quad (11)$$

$$M = \frac{bE_{ep}\varepsilon_Y h^2}{4} + \frac{2bE\varepsilon_{max}^3 R^2}{3} - \frac{bE_{ep}\varepsilon_Y^3 R^2}{3} \quad (12)$$

Let

$$M(x) = Px \text{ and } R^{-1} = v'' = \frac{\partial^2 y}{\partial x^2} \quad (13)$$

Then

$$x = A + BR^2 \text{ and } v'' = \frac{\sqrt{B}}{\sqrt{x - A}} \quad (14)$$

where

$$A = \frac{bE_{ep}\varepsilon_Y h^2}{4F} \text{ and } B = \frac{1}{F} \left(\frac{2bE\varepsilon_{max}^3}{3} - \frac{bE_{ep}\varepsilon_Y^3}{3} \right) \quad (15)$$

$$\text{Slope : } v'(x) = -2\sqrt{B}\sqrt{A - x} + g_1 \quad (16)$$

$$\text{Deflection : } v(x) = \frac{4}{3}\sqrt{B}(A - x)^{3/2} + g_1(A - x) + g_2 \quad (17)$$

Input energy. Assume that the energy input into the flexible composite beam leading to crack length a . Let boundary conditions at the end of delamination cracked part of DCB are not same as the clamped end of cantilever beam due to the ‘end of crack behaviour’. The main concern is about the range $a < X \leq X_p$ (see Figure 4), where the combined elastic and plastic deformation exists due to delamination crack at the interface. Let elastic stored energy per unit length of composite beam as e_S (along direction x with a perfect elastic condition):

For upper part

$$e_{Su} = b \int_0^{h/2} \frac{\sigma^2(y)}{2E} dy = \frac{bER\varepsilon_{max}^3}{6}; \quad 0 < |y| \leq h/2 \quad (18)$$

where ε_{max} is the maximum strain measured in the surface of composite specimen using strain gauge.

For bottom part

$$e_{Sb} = b \int_0^{y_Y} \frac{\sigma^2(y)}{2E} dy = \frac{bER\varepsilon_Y^3}{6}; \quad 0 < |y| \leq y_Y \quad (19)$$

where ε_Y is the yield strain of epoxy measured in the matrix of composite specimen using FBG sensor.

The elastic energy e_e (due to structural changes/or dissipated from delamination crack) is given by

$$e_e = b \int_{y_Y}^{h/2} \left[\frac{1}{2} \sigma_Y \varepsilon_Y + (\varepsilon - \varepsilon_Y) \sigma_Y \right] dy = \frac{bE_{ep}\varepsilon_Y}{4} \left(\frac{h^2}{2R} - h\varepsilon_Y \right); \quad y_Y < |y| \leq h/2 \quad (20)$$

The total energy expended per unit length of composite beam with a delamination, e_{total} , is

$$e_{total} = e_S + e_e = b \left(\frac{E_{ep}\varepsilon_Y h^2}{8R} - \frac{hE_{ep}\varepsilon_Y^2}{4} + \frac{ER\varepsilon_Y^3}{3} \right) \quad (21)$$

Integrating over the length x , the total energy input, E_{total} in the composite beam is equal to

$$E_{total} = E_0 + \int_a^{x_p} e_{total} dx \quad (22)$$

Fracture energy. The energy input has estimated e_{total} and is considered the energy balance for increment of the crack growth, Δa , associated with a simultaneous increase in Δv , the normal distance of the extremity of the composite beam from the initial plane³¹

$$P\Delta v = \frac{\partial E_{total}}{\partial a} \Delta a + G_C b \Delta a \quad (23)$$

Leading to

$$G_C = \frac{P}{b} \frac{\partial v}{\partial a} - \frac{1}{b} \frac{\partial E_{total}}{\partial a} \quad (24)$$

where G_C is critical fracture energy for delamination crack. Taking boundary conditions of the cantilever

beam at $x = a$, $v(a) = v'(a) = 0$, then the two constants, g_1 and g_2 , can be found, and displacement can be given as

$$v(x) = \frac{4}{3}\sqrt{B}(x-A)^{3/2} - 2\sqrt{B}\sqrt{a-A}(x-A) + \frac{2}{3}\sqrt{B}(a-A)^{3/2} \quad (25)$$

The term $\partial v/\partial a$ can be obtained from derivative of equation $v(a)$

$$\frac{\partial v}{\partial a} = \frac{a\sqrt{B}}{\sqrt{a-A}} \quad (26)$$

And derivative equation (25) to obtain $\partial E_{total}/\partial a$ value

$$\frac{\partial E_{total}}{\partial a} = b \left(\frac{E\varepsilon_{max}^3\sqrt{a-A}}{3\sqrt{B}} + \frac{E_{ep}h^2\sqrt{B}}{8\sqrt{a-A}} - \frac{E_{ep}h\varepsilon_Y^2}{4} \right) \quad (27)$$

Now, substituting values from equations (26) and (27) into equation (24), an expression for fracture energy (G_I) is obtained

$$G_I = \frac{P}{b} \frac{a\sqrt{B}}{\sqrt{a-A}} - \frac{E_{ep}\varepsilon_Y h^2\sqrt{B}}{8\sqrt{a-A}} - \frac{E\varepsilon_{max}^3\sqrt{a-A}}{3\sqrt{B}} + \frac{E_{ep}\varepsilon_Y^2 h}{4} \quad (28)$$

FBG sensors

A uniform FBG includes a segment of the optical fibre in which a periodic modulation of core refractive index is implemented. The principle of the FBG sensor is based on the shift of the centre wavelength of Bragg's grating. The spectral response of a uniform FBG in its free state as shown in Figure 7 is a signal peak centred at Bragg's wavelength λ_B as defined by Bragg's condition¹²

$$\lambda_B = 2n_{eff}\Lambda \quad (29)$$

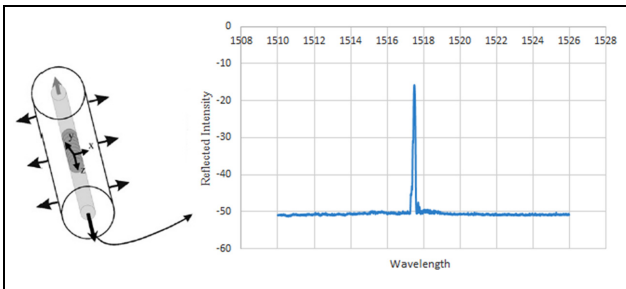


Figure 7. Spectral response of an FBG sensor at a uniform strain field.

where n_{eff} is the effective refractive index for the guided mode of interest, and Λ is the constant nominal period of the refractive index modulation. When a mechanical deformation (strain) is subjected onto a grating, it will change the effective index of refraction as well as the periodic spacing index. Bragg wavelength shift caused by the change of strain can be expressed in the form

$$\frac{\Delta\lambda_B}{\lambda_B} = \varepsilon P_e \quad (30)$$

where P_e is the strain optic coefficient and it is calculated as 0.789.

Fabrication of the specimens

Material and process

The 1 composite material examined in the present work was manufactured with twelve layers of (0/90) AR 145 E-glass Woven Roving (Colan, 398 g/m² weight and 0.5 mm thick) and Kinetix R246TX epoxy resin matrix (WC/epoxy). Mechanical properties of the materials can be seen in Table 1. The overall specimen dimensions are chosen according to ASTM D5528 standard for interlaminar fracture toughness testing. The fibre weight fraction was 60%. The specimen dimension was 400 × 400 × 5.6 mm³ and has a 50-mm-long piece of 0.001-mm-thick teflon inserted between the centre plies at one end of the specimen to create a pre-crack, a_0 .

One of the advantages of FBG sensors is the ability to embed in between fibre layers because of its small size. However, an especial care needs to be taken to protect the sensor during the fabrication process. A FBG sensor with grating length of 5 mm (SMF-280 fibre-type with centre wavelength (λ_b) equal to 1548 ± 0.3 nm) was embedded between the first and second layers above the centreline of the laminate. The FBG sensor is coated with acrylate. However, the coating around the grating location was stripped off before embedding it inside the composite. The FBG sensor was located approximately 5–6 mm from the delamination plane as shown in Figure 8.

The influence of the curing process of the laminate on the FBG sensor was observed. The description of the FBG spectra before and after embedding is shown in Figure 9. After embedding, the reflected FBG spectra were splitting into two peaks and shifted to the left. This distortion of spectra was caused by the effect of the transverse strain during the curing. The transverse strain is the induced residual strain that promotes certain birefringence in the core of the fibre and the geometry of the fibre. Because of the axial strain, the wavelength of the sensor was shifted. It has been observed that the wavelength of the FBG spectra has shifted about 0.061 nm as shown in Figure 10.

Table 1. Mechanical properties for $[0/90]_{12}$ WC/epoxy specimen.

Materials	E11 (GPa)	E22 (GPa)	E33 (GPa)	ν_{12}	ν_{13}	ν_{23}	G12 (GPa)	G13 (GPa)	G23 (GPa)	σ fracture (MPa)
Epoxy	2.435			0.29						77.8
WC/epoxy composite	15	15	9.5	0.126	0.126	0.263	6.527	6.527	7	245

WC: woven cloth.

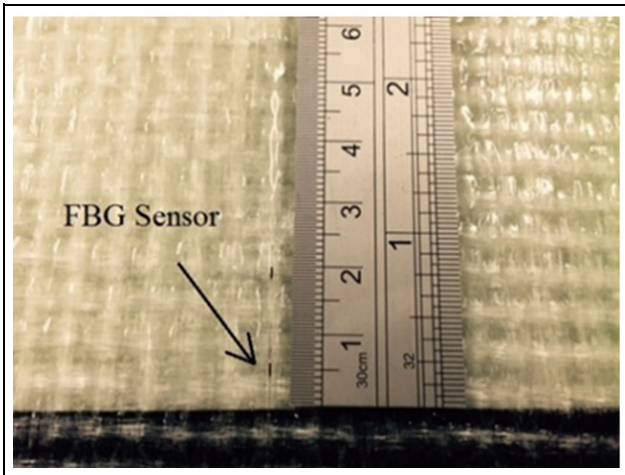


Figure 8. Location of embedding FBG sensor in the specimen.

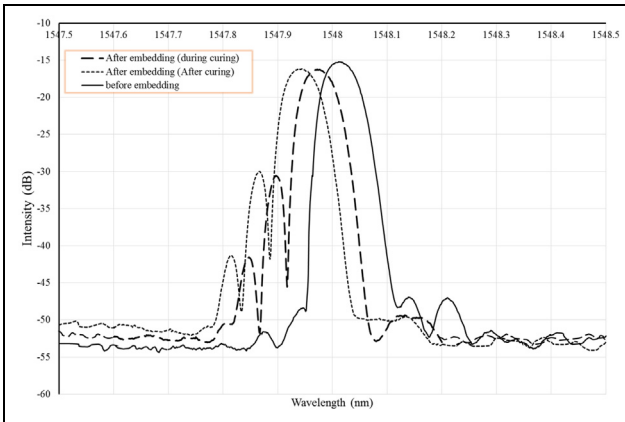


Figure 9. Comparison of reflected FBG spectra before and after curing.

DCB specimen

A DCB specimen was cut from the plate using a computer numerical control water jet cutter. The dimension of the DCB sample was 210 mm × 30 mm, and composite tabs of 30 mm × 10 mm × 10 mm were attached as shown in Figure 11. Eight samples were prepared for testing. DCB test was performed on two

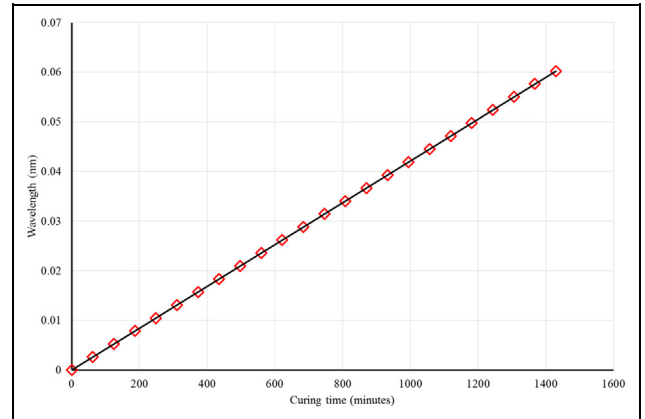


Figure 10. FBG wavelength shift during curing process.

groups of specimens. The first group contained five specimens numbered SD1, SD2, SD3, SD4 and SD5. These specimens have no embedded FBG sensors. This group of specimens was tested at loading rates ranging from 1 to 1.5 mm/min. The second group of specimens contained three specimens SDF1, SDF2 and SDF3, and each sample have an embedded FBG sensor. The second group of the specimen was tested at the same loading rates as the first group of specimens and stopped intermittently for the FBG signal measurements. The FBG signal has been used to find the yield strain (ϵ_Y) accurately.

Electrical resistance foil strain gauges were attached to the sample surface at 5 mm distances from the end of initial delamination to measure the surface strains. The purpose of these strain gauges was to measure the maximum strain (ϵ_{max}) at the surface of the specimen.

Experimentation

Interlaminar fracture toughness tests

DCB tests were performed according to ASTM D5528 standard to determine interlaminar fracture toughness. A 10-kN uniaxial MTS testing machine was used for loading the specimen. Modified compliance calibration method (ASTM D5528) was used for reduction of test data for Mode I delamination. The displacement Δ mm

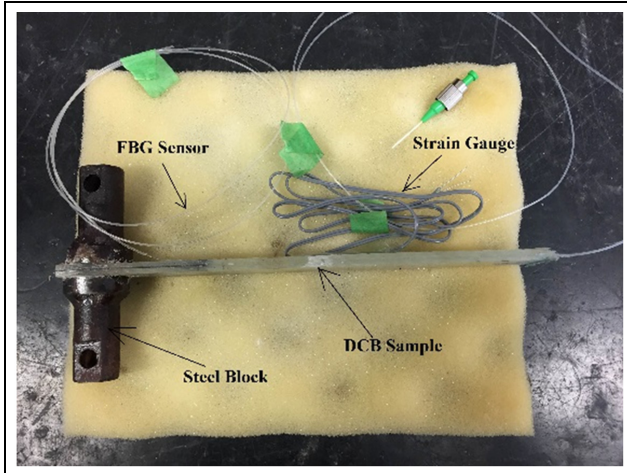


Figure 11. DCB specimen of $[0/90]_{12}$ WC/epoxy with embedding FBG sensor and bonding strain gauge.

was increased at a rate of 1.5 mm/min. The crack tip was continuously monitored with Casio Exilim EX-FH20 high-speed camera that records up to 1000 frames per second, and the time was recorded with the crack tip position (Figure 12). The specimens which have embedded FBG sensors were loaded at a rate of 1.5 mm/min and stopped intermittently in order to take measurements of the FBG sensor response. After that, the specimen was reloaded to next load level.

The thickness side of specimens was polished and marks were drawn at 1-mm intervals for first 5 mm and at 5-mm intervals for 20 mm as shown in Figure 13. The crack propagation was measured using the high-speed camera. The values of P and Δ were measured and stored for each crack increment $\Delta a = 1$ mm. The specimen with extended open cracks is shown in Figure 13.

FEA – cohesive zone model for Mode I delamination

A finite element model of the tested specimen was created in Abaqus 6.13 to analyse and simulate Mode I delamination growth. Double node ‘Cohesive’ elements were used to represent the bonded interfaces. The specimen geometry is depicted in Figure 14. A purposely created 50-mm-long delamination was also created in the model as the test specimen configuration.

The specimen geometry was meshed using 3D solid elements C3D8I with the top and bottom parts of the specimen. Each part was separately meshed using different mesh sizing. Disbonded interfaces were defined in the middle of the specimen and represent the delamination surface of the test specimen (Figure 15).

Delamination growth was simulated using 0.001-mm-thick cohesive elements COH3D8 created at the interfaces. The user-cohesive element technique was implemented by means of use material subroutine (UMAT) subroutine. Autodesk[®] Simulation Composite Analysis 2015 Plug-ins[®] for Abaqus 6.13 was used to create the UMAT subroutine to calculate the nine state damage variables (SDV_n) for the cohesive materials. These state damage variables are stored by Abaqus at each individual integration point within the finite element model. Two state variables are used in this study to indicate the damage. SDV_2 which is a continuous real variable between zero and one that indicates the damage initiation is satisfied. SDV_6 is the damage variable, a continuous real variable, that varies between zero and one.

Results and discussion

Load–displacement response

The measured load–displacement curves for all specimens tested are shown in Figure 16. Each point on the

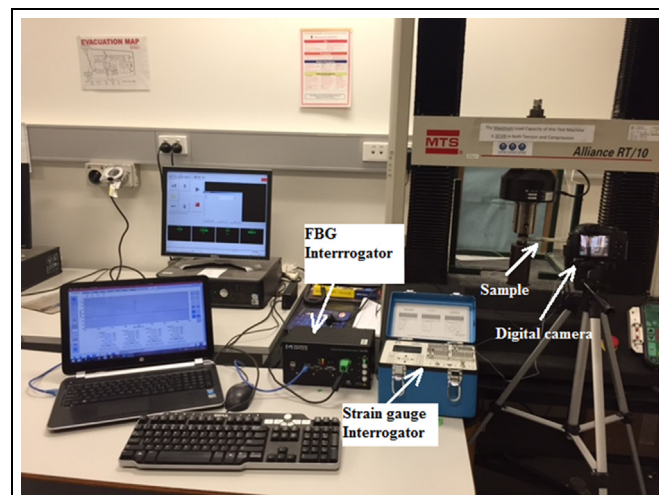


Figure 12. The configuration of the test rig.

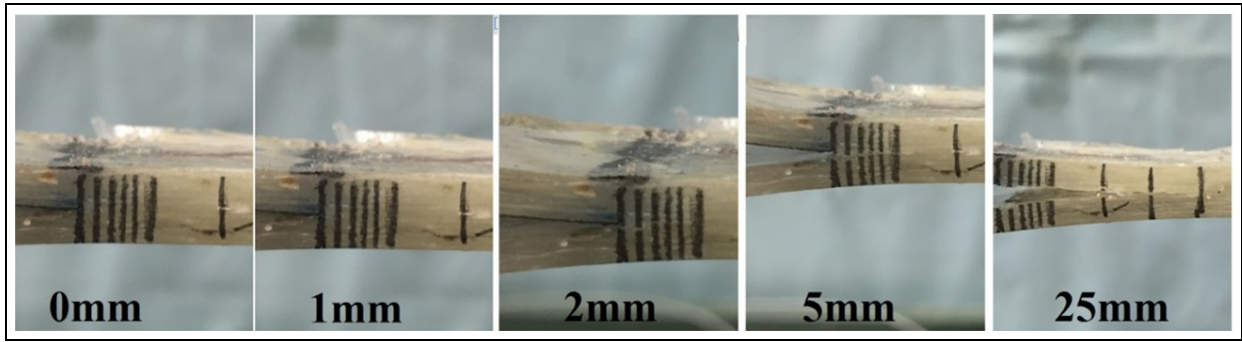


Figure 13. Propagating delamination cracks during DCB test in various displacement for $[0/90]_{12}$ WC/epoxy.

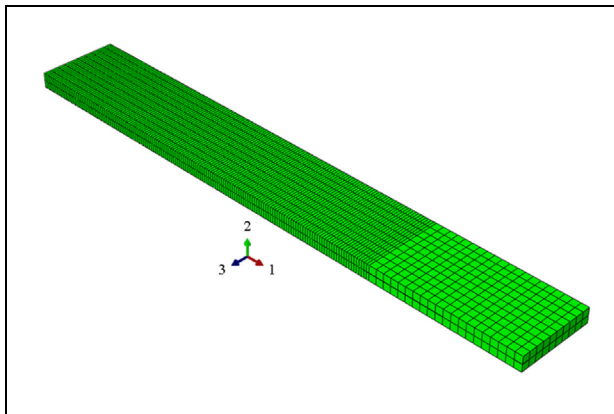


Figure 14. DCB specimen finite element model.

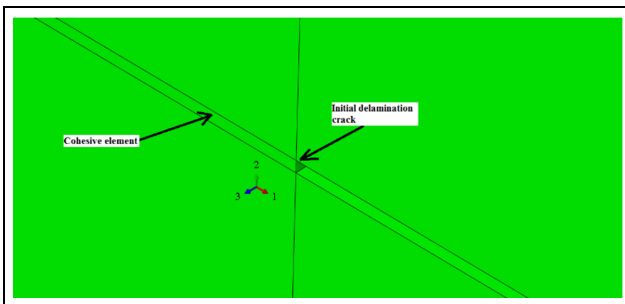


Figure 15. A cohesive element in finite element model.

curves corresponds to crack increment $\Delta a = 1$ mm for the first 5 mm and $\Delta a = 5$ mm for the next 20-mm length. These curves were used for calculating R -curve ($G(a)$). Although there is a deviation in the curves, they generally follow a similar behaviour. This deviation found in the curves is due to the different elastic responses of the specimens. As Figure 16 shows, P - Δ curves follow the same behaviour of the delamination crack. The load (P) has increased linearly until onset of delamination crack. After that, the load (P) increases

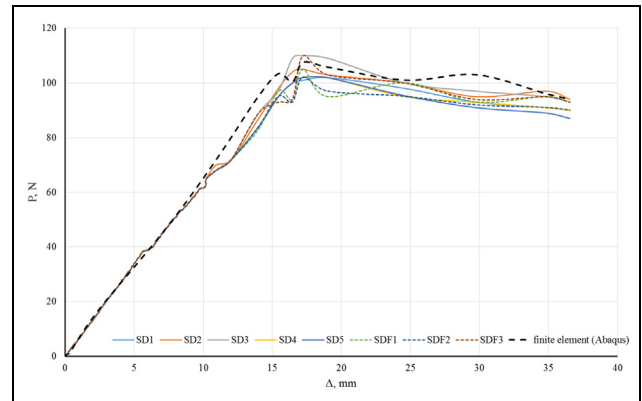


Figure 16. Force–displacement measurements for DCB specimens with (solid lines) and without (dash lines) embedded FBG sensors for $[0/90]_{12}$ WC/epoxy specimen.

constantly when delamination crack starts propagation. At the final stage of the crack propagation, there is a significant fluctuation in the curve due to non-uniform propagation process of the crack. This behaviour can be attributed to the woven pattern of the composite layer.³ The fluctuation in P - Δ curve may have affected on the accuracy of calculation R -curves and fracture energy (G) of woven composite.

Initiation and propagation of delamination crack

Mode I delamination crack was examined under a microscope to investigate the initiation and propagation of delamination. Figure 17 shows the nature of delamination damage growth in the specimen during the test. The microscope investigation shows two different regions related to delamination crack spots. Region (I) is the initiation of delamination damage region. In Region (I) of Figure 17, the matrix cracking is identified as primary damage region. This region contains brighter regions than the surrounding area due to microcrack growth within the matrix layer. These

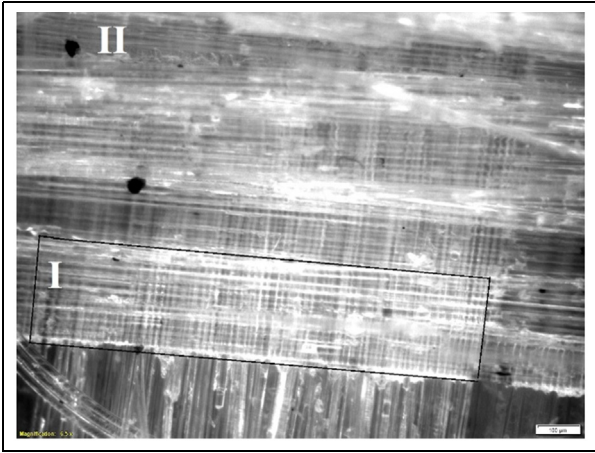


Figure 17. Microscopic view of a DCB test specimen: brighter microcrack spots (Region I) and propagation of delamination crack (Region II).

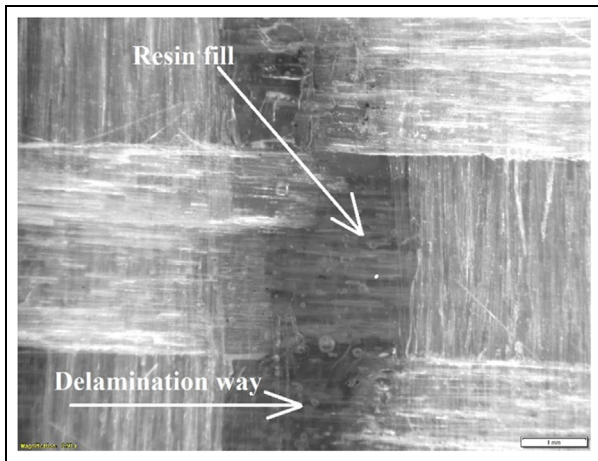


Figure 18. Microscopic view of a DCB test specimen shows the behaviour of delamination crack.

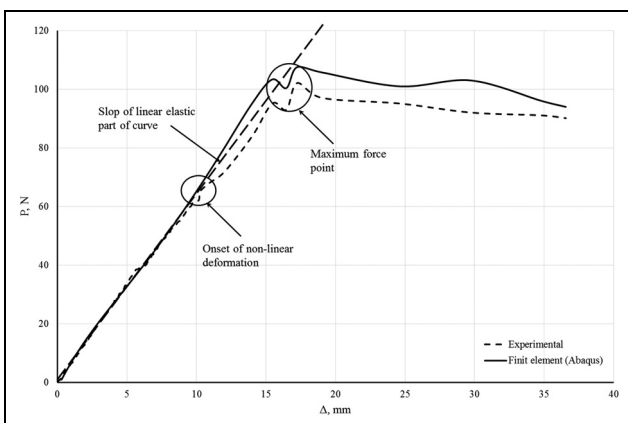


Figure 19. Load–displacement curve (hidden line is experimental results; the solid line is finite element result) for [0/90]₁₂WC/epoxy specimen.

microcracks cause stress concentration in the interface region around the crack tip. With the increase in loading, coalesce of microcracks occurs. Coalesce of these microcracks are driving the delamination crack. Region (II) in Figure 17 shows delamination crack propagation along the interfaces of the matrix and the WC fibre layer. Furthermore, Figure 18 shows the delamination crack propagation which is specific to WC fibre layers. The microscopic investigation of a delamination crack (Figure 18) shows two different regions. The first region is a bright region due to a delamination crack. The second region is a resin-fill region (dark region). A close examination of the microscopic examinations shows a discontinuity in delamination crack propagation which causes ‘jumping’ behaviour of the crack propagation in woven composite layers.

As shown in Figure 19, slope of linear elastic part of the P - Δ curve is drawn to determine the starting point of non-linear deformation. The starting point also used for defining the initiation of delamination crack and the fracture energy G_{IOnset} . Figure 19 indicates the onset and propagation of delamination crack in the sample SDF2 and the FEA results. At Δ is equal to 10.23 mm and the load is equal to 65 N, the elastic property of the sample starts to change from linear to non-linear indicating the propagation of delamination crack. After reaching the maximum force around 110 kN, the load remains constant because the specimen stiffness has been changed due to the delamination crack growth. All the specimens have shown a similar trend. A summary of the G_{IOnset} , G_{IC} using ASTM equation (equation (5)), the force onset of delamination crack (P_{Onset}) and displacement onset of delamination crack (Δ_{Onset}) are shown in Table 2.

FBG sensors' strain measurements

Responses of embedded FBG sensor were measured and stored in two forms, peak wavelength and the reflected spectrum. As shown in Figure 20, wavelength shifts increase with the applied displacement. There is a significant increase in spectral response at 17.23-mm imposed displacements. This change is an indication of the initiations of a number of damages in the specimen. The FBG sensor was embedded about 5–6 mm from the tip of the initial delamination crack; thus, the change of reflected spectra at 17.23-mm imposed displacement can be due to the initiation of delamination crack. The change of FBG wavelength was compared with the corresponding point of load–displacement curve (Figure 19). The comparison shows that the changes in the P - Δ curve and the wavelength of FBG sensor occurred at 17.23-mm imposed displacements. This observation has confirmed that the significant

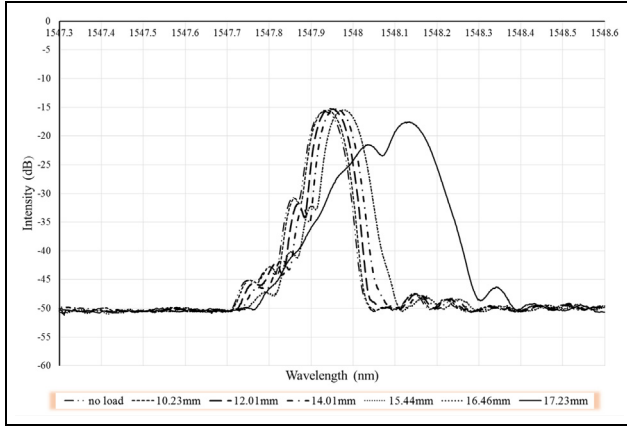


Figure 20. Spectra of embedded FBG in WC/epoxy specimen under Mode I delamination test with increasing displacement.

Table 2. Load and G result for WC/epoxy specimens (laminate configuration is $[0/90]_{12}$ WC/epoxy and $400 \times 400 \times 5.6 \text{ mm}^3$).

Sample	P_{Onset} (N)	Δ_{Onset} (mm)	G_{IOnset}	G_{IC}
SD1	65.45	10.412	0.227	0.413
SD2	65.23	10.265	0.219	0.400
SD3	65.57	10.430	0.233	0.426
SD4	65.49	10.427	0.234	0.421
SD5	65.21	10.231	0.223	0.410
SDF1	65.454	10.416	0.230	0.414
SDF2	65.52	10.424	0.231	0.428
SDF3	65.32	10.341	0.224	0.435
Finite element	65.58	10.418	0.238	0.447

WC: woven cloth.

change in the FBG spectral response is a definite indication of the initiation of a delamination crack.

While the delamination crack was growing, the centre wavelength of the FBG was shifting and the spectra are chirping (Figure 20). After 17.23-mm imposed displacements, the FBG signal has shifted to leftward because the crack tip was reasonably away from the FBG sensor.

The second step in the elasto-plastic method is to evaluate changes in local strain during crack initiation and propagation of the delamination crack. Equation (30) was used to calculate the strain in the plane of delamination crack. The local strain results obtained from FBG sensor during the test are shown in Figure 21. These results show that the local strain in the plane of delamination crack has three regions. The first strain region is the elastic range. Before the crack onset, the strain increases with the increase in applied displacement. With the increase in displacement, the strain–displacement curve has changed from linear to non-linear behaviour. The main cause for this change

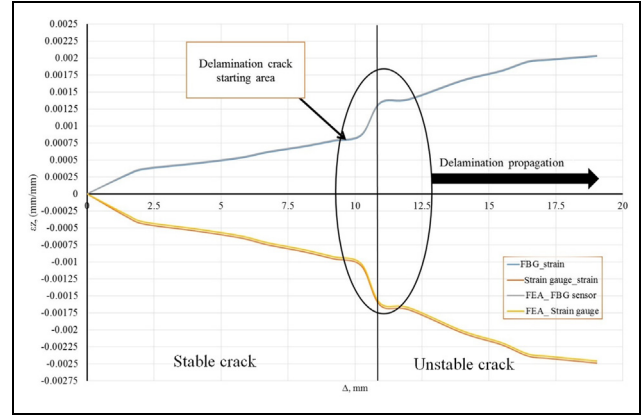


Figure 21. Strain–displacement relationship with increasing delamination cracks for WC/epoxy specimen.

can be attributed to the elasto-plastic behaviour of epoxy resin. By a close inspection of Figure 22, elastic–plastic strain and plastic stress field in the epoxy material can be identified. As a consequence, the status of this region can be declared as an elastic–plastic. Interestingly, the strain is increasing linearly until it arrives to 10.23-mm imposed displacements. The strain at the onset of delamination crack is $1350 \mu\epsilon$, which was measured by the FBG sensor. The corresponding stress is 101 MPa ($\sigma = E_{ep}\epsilon$). The chirped spectral response of the FBG sensor indicates that the local matrix strain at the plane of the delamination crack is the most appropriate measurement for calculation of stress at the crack tip. The interface failure stress is considerably smaller than the failure stress at the composite specimen, which is equal to 245 MPa as shown in Table 1. However, according to Figure 19, the delamination crack is onset at 101 MPa. Then, Figure 21 can be divided into two regions, stable crack and unstable crack, according to imposed critical displacement of 10.23 mm. At critical imposed displacement, the strain at FBG sensor location was measured as 0.00075 mm/mm. Thereafter, the delamination crack is onset at 0.00125 mm/mm strain value. Finally, the crack becomes unstable after 0.00175 mm/mm strain value and delamination crack being propagated. The strain fields at the embedded FBG sensor were simulated and evaluated using FEA. As shown in Figure 23(a) and (b), FEA results have an excellent correlation with strain readings obtained from the FBG sensor experimentally.

Calculation of R-curve

The fracture energy G_I as a function of delamination crack propagation can be evaluated using both equations (5) and (28) and FBG strain readings. As shown

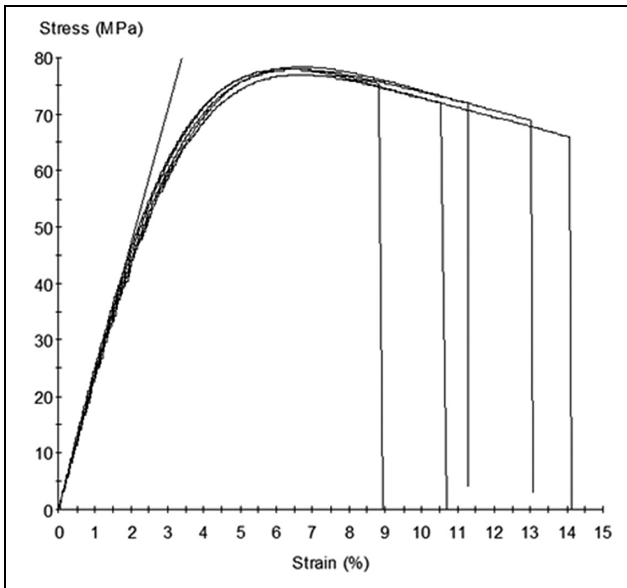


Figure 22. Stress–strain diagram (tensile test) for neat epoxy.

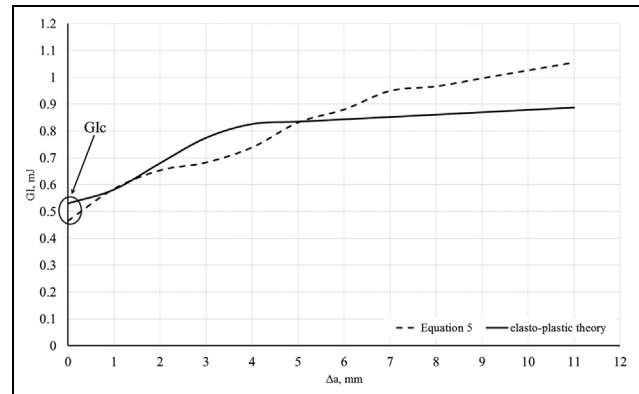


Figure 24. Experimental R -curve as a function of delamination crack length and strain for $[0/90]_{12}$ WC/epoxy specimen.

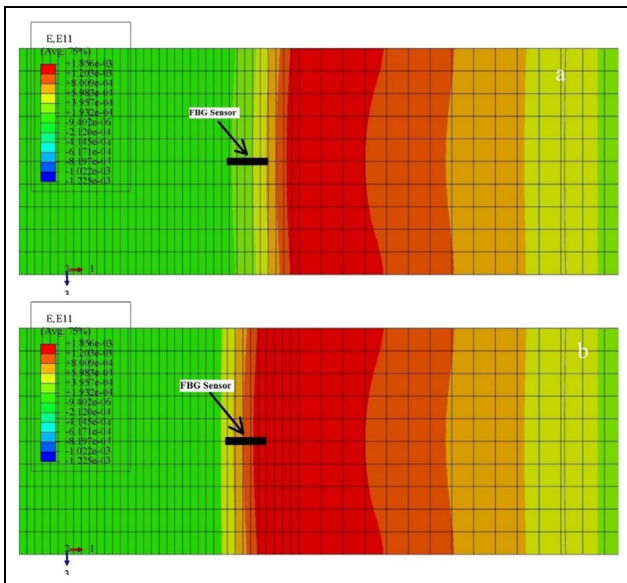


Figure 23. Strain field at FBG sensor in finite element model for WC/epoxy at imposed displacement: (a) at 10.23 mm and (b) at 17.23 mm.

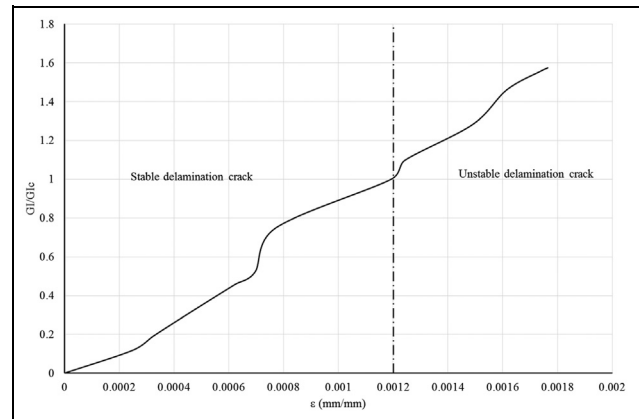


Figure 25. Examining stability of delamination crack Mode I depending on G_I/G_{IC} ratio, and strain measuring from FBG sensor for $[0/90]_{12}$ WC/epoxy specimen.

in Figure 24, R -curve is calculated after delamination crack was extended to 10 mm because the FBG sensor was embedded about 5–6 mm away from the purposely created delamination crack. The calculations of G_{IC} showed that both equations have provided similar results for this region. However, R -curves which were calculated from equations (5) and (28) have shown some differences when the crack is propagating. This difference is due to equation (5), which is valid for

isotropic materials and linear crack propagation cases. Hence, equation (5) may not be suitable for R -curve calculations of WC/epoxy composite materials.

The stability of delamination crack can be estimated utilizing G_I/G_{IC} ratios and FBG sensor strain values. This estimate is presented in Figure 25. The delamination crack is stable when the ratio G_I/G_{IC} is less than 1. The delamination growth is monotonically increasing with the increase in imposed displacement (Δ), as anticipated. However, the crack is unstable when the G_I/G_{IC} ratio is equal or greater than 1.

Elasto-plastic model (equation (28)) and equation (5) were used to calculate R -curves for different laminated composite materials for comparison. The mechanical properties of all composite materials were used for calculation shown in Table 3 and the P - Δ curve shown in Figure 26. As shown in Figure 26, all composite materials exhibit an onset of delamination (initiation of non-

Table 3. Mechanical properties for different composite materials.

Materials	E_{11} (GPa)	E_{22} (GPa)	E_{33} (GPa)	ν_{12}	ν_{13}	ν_{23}	G_{12} (GPa)	G_{13} (GPa)	G_{23} (GPa)	G_I (mj)	Type of material	Reference
GF/PCBT	14.73	14.73	10.9	0.25	0.5	0.5	1.789	1.43	1.43	1.5	Woven 0/90	Yang et al. ³²
CF/PCBT	25.7	25.7	15.9	0.2	0.35	0.35	3.5	1.43	1.43	1.5		Kakei et al. ²⁷
WC/epoxy	15	15	9.5	0.126	0.126	0.26	6.527	6.527	7	0.414		Samborski ³³
H5160RM	109	8.819	8.819	0.342	0.342	0.38	4.315	4.315	3.2	0.4	Unidirectional 0	Soto et al. ³⁴
T300/977-2	150	11	11	0.25	0.25	0.45	6	6	3.7	0.352		

WC: woven cloth; GF: Glass woven fabric; CF: Carbon woven fabric; PCBT: Polymerized poly butylene terephthalate.

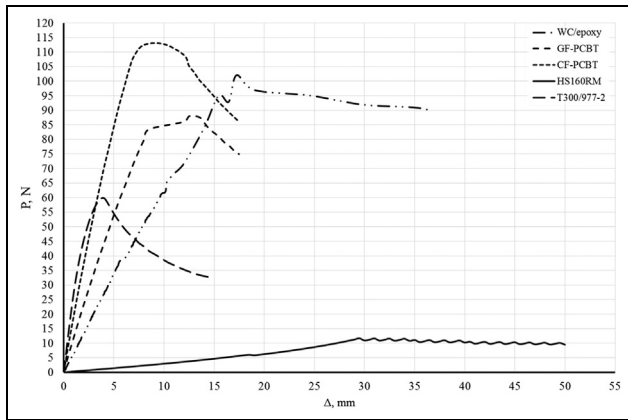


Figure 26. Force–displacement measurements for DCB specimens for different composite materials.

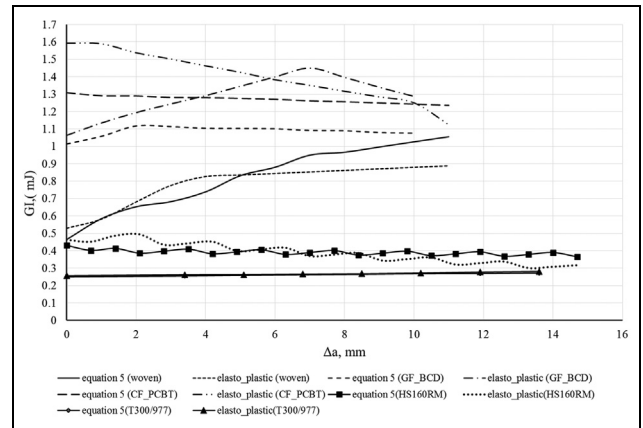


Figure 28. Experimental R -curve as a function of delamination crack length and strain.

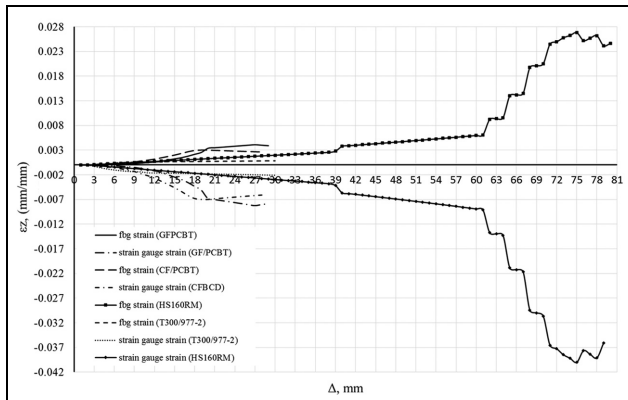


Figure 27. Strain–displacement relationship with increasing delamination cracks.

linear deformation range) point. This point has different values and depends on mechanical properties (elasticity, cohesive and wave geometry) of composite materials. The initiation of delamination in Figure 27 is the second region after linear (elastic) strain region. FEA has been used to simulate the local strain at the location of FBG sensor and strain at the surface of the

specimen. Figure 28 shows R -curves for tested composite materials. The result shows that equation (5) and elasto-plastic model (equation (28)) have same R -curve value and behaviour for unidirectional composite materials. As anticipated, the R -curves from equations (5) and (28) are significantly different for the WC composite materials. However, R -curves calculated from equations (5) and (28) for unidirectional composites have shown some similarities.

The R -curve ($G(a)$) is calculated from state damage variables SDV2 and SDV6 and the strain at FBG sensor location at FEA strain plots, which are shown in Figures 29–31. SDV2 value is obtained for FBG sensor and surface-mounted strain gauge positions. The interface cohesive elements were used to calculate the load–displacement curve $P(\Delta)$ and R -curve ($G(a)$) for the specimens. Mode I delamination was evaluated by FEA simulation. The nine state damage variables (SDV1, SDV2, ..., SDV9) were used as a criteria to evaluate crack onset and the cohesive elements for crack surface (see Figure 29). As shown in Figures 30 and 31, the state damage variables SDV2 and SDV6 before the “imposed displacement 10.23 mm” in Mode I, is almost zero. When the crack propagated beyond 10.23-mm imposed

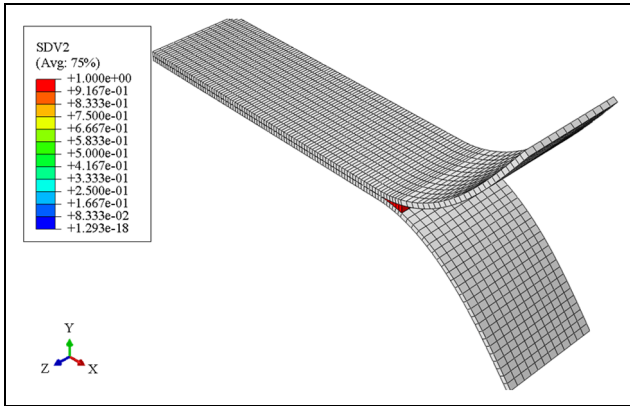


Figure 29. SDV2 values with developing crack delamination in cohesive element model.

displacement, the set values of SDV2 and SDV6 are equal to 1. That means the crack in the specimen is dynamic and the delamination being propagated. The finite element result was compared with the experimental observations that are captured by the high-speed camera. The comparison shows that the cohesive element model gives accurate results and its results are close to the experimental observations especially at the crack onset point.

Conclusion

In this study, a FBG sensor has been used to monitor and evaluate the Mode I delamination behaviour of laminated composites. A mathematical model based on elastic–plastic process at the matrix interface was established to evaluate fracture energy (G) of delamination damage propagation. Load onset of delamination crack and critical strain were calculated using embedded FBG sensor response and surface-attached strain gauge.

Subsequently, FEA was performed using cohesive elements to simulate delamination process. The state damage variables, SDV2 and SDV6, were calculated to evaluate damage status.

Apparent changes in the reflected FBG sensor spectrum have indicated the development of a delamination crack between layers. This distortion of spectra was caused by the effect of the non-uniform strain due to the tip of delamination crack which promoted non-uniform fringing in the core of the fibre.

The elasto-plastic theory has been applied on different unidirectional and WC-laminated composite materials. The proposed theory was used to obtain two parameters, that is, to estimate critical fracture energy (G_{IC}) and to calculate R -curve. The results from the proposed theory (G_{IC}) have shown a good agreement with the G_{IC} values estimated by ASTM D5528 (equation (5)). However, noticeable differences were observed for R -curve calculated by the proposed theory and the ASTM D5528 (equation (5)). This difference in G values can be attributed to the limitation of ASTM D5528 (equation (5)) standard procedures which developed from ideal isotropic cantilever beam. Moreover, the effect of woven yarns and ‘damage jump’ in WC-laminated composites have caused many discrepancies to the damage propagation process. Interestingly, the differences in G values of the proposed theory and the ASTM D5528 (equation (5)) standard procedures were not observed in unidirectional laminated composite materials.

The finite element simulation using cohesive element technique has shown a good correlation with experimental results, that is, P - Δ curve and strain at FBG sensor locations. The state damage variables (SDV n) in Abaqus 6.13 FEA software have demonstrated the capability of verification and validation of Mode I delamination.

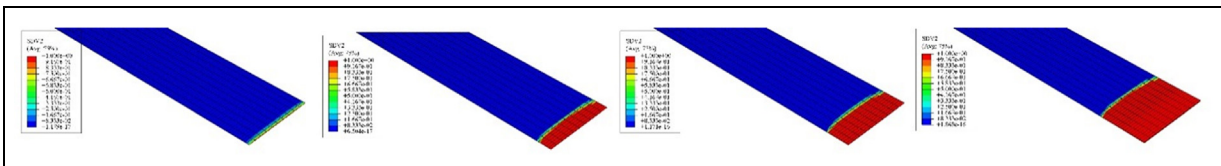


Figure 30. SDV2 developing in cohesive elements with increasing displacement.

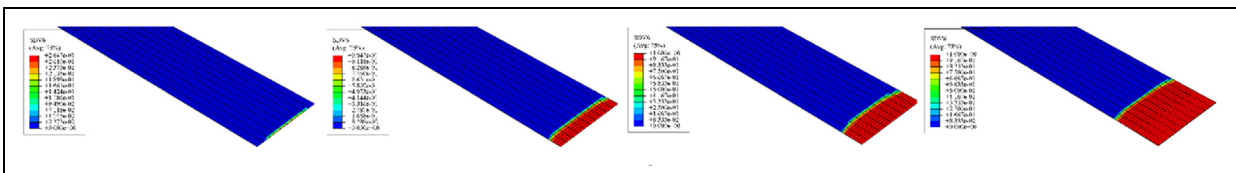


Figure 31. SDV6 developing in cohesive elements with increasing displacement.

Finally, it can be concluded that the proposed elasto-plastic model has accurately predicted Mode I delamination crack propagation in laminated composites reinforced with woven glass fibres. The embedded FBG sensor has provided accurate information about the damage status and the strain measurements to calculate essential parameters G_{IC} and R -curve. However, this model needs to be fine-tuned to include fracture Modes II and III for more robust predictions of structures under multi-axial loading. Furthermore, it can be concluded that the ‘Cohesive Element’ in Abaqus software has proved its ability to simulate delamination growth in composite materials.

Declaration of conflicting interests

The author(s) declared no potential conflicts of interest with respect to the research, authorship and/or publication of this article.

Funding

The author(s) received no financial support for the research, authorship and/or publication of this article.

References

1. Kakei AAG, Epaarachchi KJA, Islam MM, et al. Development of fracture and damage modeling concepts for composite materials. In: Epaarachchi JA and Kahandawa GC (eds) *Structural health monitoring technologies and next-generation smart composite structures*. Boca Raton, FL: CRC Press, 2016, pp. 339–364.
2. Pawar PM and Ganguli R. Modeling progressive damage accumulation in thin walled composite beams for rotor blade applications. *Compos Sci Technol* 2006; 66: 2337–2349.
3. Suppakul P and Bandyopadhyay S. The effect of weave pattern on the mode-I interlaminar fracture energy of E-glass/vinyl ester composites. *Compos Sci Technol* 2002; 62: 709–717.
4. Pereira AB, de Morais AB, de Moura MFSF, et al. Mode I interlaminar fracture of woven glass/epoxy multi-directional laminates. *Compos Part A: Appl S* 2005; 36: 1119–1127.
5. Ying X, Christopher L, Zhenglin Y, et al. A new fiber optic based method for delamination detection in composites. *Struct Health Monit* 2003; 2: 205–223.
6. Alfredo G, Antonio F-L and Soller BJ. Optical fiber distributed sensing – physical principles and applications. *Struct Health Monit* 2010; 9: 233–245.
7. Yashiro S, Takeda N, Okabe T, et al. A new approach to predicting multiple damage states in composite laminates with embedded FBG sensors. *Compos Sci Technol* 2005; 65: 659–667.
8. Sans D, Stutz S, Renart J, et al. Crack tip identification with long FBG sensors in mixed-mode delamination. *Compos Struct* 2012; 94: 2879–2887.
9. Okabe T and Yashiro S. Damage detection in holed composite laminates using an embedded FBG sensor. *Compos Part A: Appl S* 2012; 43: 388–397.
10. Takeda S, Okabe Y and Takeda N. Delamination detection in CFRP laminates with embedded small-diameter fiber Bragg grating sensors. *Compos Part A: Appl S* 2002; 33: 971–980.
11. Takeda S, Minakuchi S, Okabe Y, et al. Delamination monitoring of laminated composites subjected to low-velocity impact using small-diameter FBG sensors. *Compos Part A: Appl S* 2005; 36: 903–908.
12. Sorensen L, Botsis J, Gmür T, et al. Delamination detection and characterisation of bridging tractions using long FBG optical sensors. *Compos Part A: Appl S* 2007; 38: 2087–2096.
13. Stutz S, Cugnoni J and Botsis J. Studies of mode I delamination in monotonic and fatigue loading using FBG wavelength multiplexing and numerical analysis. *Compos Sci Technol* 2011; 71: 443–449.
14. Kahandawa GC, Epaarachchi J, Wang H, et al. Extraction and processing of real time strain of embedded FBG sensors using a fixed filter FBG circuit and an artificial neural network. *Measurement* 2013; 46: 4045–4051.
15. Kahandawa GC, Epaarachchi JA, Wang H, et al. Use of fixed wavelength fibre-Bragg grating (FBG) filters to capture time domain data from the distorted spectrum of an embedded FBG sensor to estimate strain with an artificial neural network. *Sensor Actuat A: Phys* 2013; 194: 1–7.
16. Kakei A, Epaarachchi JA, Islam M, et al. Integrated FBG sensor response and full field thermoelastic stress approach to monitor damage accumulation in glass fibre reinforced composite plate. In: *Proceedings of the 10th international workshop on structural health monitoring*, Stanford University, Stanford, CA, 1–3 September 2015.
17. Yu F, Wu Q, Okabe Y, et al. The identification of damage types in carbon fiber-reinforced plastic cross-ply laminates using a novel fiber-optic acoustic emission sensor. *Struct Health Monit* 2016; 15: 93–103.
18. Jokinen J, Wallin M and Saarela O. Applicability of VCCT in mode I loading of yielding adhesively bonded joints – a case study. *Int J Adhes Adhes* 2015; 62: 85–91.
19. Shokrieh MM, Rajabpour-Shirazi H, Heidari-Rarani M, et al. Simulation of mode I delamination propagation in multidirectional composites with R-curve effects using VCCT method. *Comput Mater Sci* 2012; 65: 66–73.
20. Bonhomme J, Argüelles A, Viña J, et al. Numerical and experimental validation of computational models for mode I composite fracture failure. *Comput Mater Sci* 2009; 45: 993–998.
21. Shor O and Vaziri R. Adaptive insertion of cohesive elements for simulation of delamination in laminated composite materials. *Eng Fract Mech* 2015; 146: 121–138.
22. Wang C and Xu X. Cohesive element analysis of fatigue delamination propagation in composite materials with improved crack tip tracking algorithm. *Compos Struct* 2015; 134: 176–184.
23. Barenblatt G. The mathematical theory of equilibrium cracks in brittle fracture. *Adv Appl Mech* 1962; 7: 55–129.

24. Shanmugam V, Penmetsa R, Tuegel E, et al. Stochastic modeling of delamination growth in unidirectional composite DCB specimens using cohesive zone models. *Compos Struct* 2013; 102: 38–60.
25. Saeedifar M, Fotouhi M, Ahmadi Najafabadi M, et al. Prediction of delamination growth in laminated composites using acoustic emission and cohesive zone modeling techniques. *Compos Struct* 2015; 124: 120–127.
26. Haselbach PU, Bitsche RD and Branner K. The effect of delaminations on local buckling in wind turbine blades. *Renew Energ* 2016; 85: 295–305.
27. Kakei A, Epaarachchi JA, Islam M, et al. Detection and characterisation of delamination damage propagation in woven glass fibre reinforced polymer composite using thermoelastic response mapping. *Compos Struct* 2016; 153: 442–450.
28. Chen D and El-Hacha R. Cohesive fracture study of a bonded coarse silica sand aggregate bond interface subjected to mixed-mode bending conditions. *Polymers* 2014; 6: 12–38.
29. Lekhnitskii SG. *Anisotropic plates*. New York: Gordon and Breach Science Publishers, 1968.
30. Reddy JN. *Mechanics of laminated composite plates and shells: theory and analysis*. Boca Raton, FL: CRC Press, 2004.
31. Chauffaille S, Jumel J and Shanahan MER. Elasto-plastic analysis of the single cantilever beam adhesion test. *Eng Fract Mech* 2011; 78: 2493–2504.
32. Yang B, Wang Z, Zhou L, et al. Experimental and numerical investigation of interply hybrid composites based on woven fabrics and PCBT resin subjected to low-velocity impact. *Compos Struct* 2015; 132: 464–476.
33. Samborski S. Numerical analysis of the DCB test configuration applicability to mechanically coupled fiber reinforced laminated composite beams. *Compos Struct* 2016; 152: 477–487.
34. Soto A, González EV, Maimí P, et al. Cohesive zone length of orthotropic materials undergoing delamination. *Eng Fract Mech* 2016; 159: 174–188.